Title

Designing Heteroatom-Codoped Iron Metal—Organic Framework for Promotional Photoreduction of Carbon Dioxide to Ethylene

Journal

Angewandte Chemie International Edition, 62(14)

ISSN

1433-7851

Authors

Guo, Fan

Li, Rui-Xia

Yang, Sizhuo

et al.

Publication Date

2023-03-27

DOI

10.1002/anie.202216232

Designing Heteroatom-Codoped Iron Metal–Organic Framework for Promotional Photoreduction of Carbon Dioxide to Ethylene

Fan Guo,*[a],[b] Rui-Xia Li,[a] Sizhuo Yang,[c] Xiao-Yu Zhang,[b] Hongjian Yu,[a] Jeffrey J. Urban,[c] and Wei-Yin Sun*[b]

[a] Dr. F. Guo, R.-X. Li, Dr. H. Yu
School of Chemistry and Chemical Engineering, Yangzhou University
Yangzhou 225002 (P. R. China)
E-mail: guofan@yzu.edu.cn

[b] Dr. F. Guo, X.-Y. Zhang, Prof. Dr. W.-Y. Sun
Coordination Chemistry Institute, State Key Laboratory of Coordination Chemistry, School of Chemistry and Chemical Engineering, Nanjing National Laboratory of Microstructures, Collaborative Innovation Center of Advanced Microstructures, Nanjing University
Nanjing 210023 (P. R. China)
E-mail: sunwy@nju.edu.cn

[c] Dr. S. Yang, Prof. Dr. J. J. Urban
The Molecular Foundry, Lawrence Berkeley National Laboratory
1 Cyclotron Rd, Berkeley, California 94720 (USA)

Supporting information for this article is given via a link at the end of the document.

Abstract: Rational engineering active sites and vantage defects of catalysts are promising but grand challenging task to enhance photoreduction CO_2 to high-value-added C2 products. In this study, we designed a N,S codoped Fe-based MIL-88B catalyst with well-defined bipyramidal hexagonal prism morphology via a facile and effective process, which was controllably synthesized by addition of appropriate 1,2-benzisothiazolin-3-one and acetic acid to the reaction solution. Under simulated solar irradiation, the designed catalyst exhibits high C_2H_4 evolution yield of 17.7 μmol/g·h, which has been rarely achieved in photocatalytic CO_2 reduction process. The synergistic effect of Fe−N coordinated sites and reasonable defects in the N,S codoped photocatalyst can accelerate the migration of photogenerated carriers, which would result in high electron density, and this in turn helps to facilitate the formation and dimerization of C–C coupling intermediates for C_2H_4 effectively.

Introduction

Solar-driven CO_2 reduction into value-added feedstock is a win-win route to mitigate the depletion of energy and alleviate the greenhouse gas emission.[1] In the recent decade, owing to the intriguing architectures, preferable stability, excellent durability, and tailored functionality, diverse metal−organic frameworks (MOFs) have captured considerable attention as photocatalysts, which can catalyze CO_2 to two electrons reduced C1 product CO and HCOOH, and further multi-electrons reduced hydrocarbons CH_4 and CH_3OH.[2] C_2H_4, a high-valued multicarbon hydrocarbon product for producing diversified plastics and cosmetics, is generally derived from steam cracking of naphtha under very strict conditions (800–900 °C).[3] Numerous attempts, especially electrocatalytic route, have been made to obtain C_2H_4 via CO_2 reduction reaction due to its highly commercioganic and practical applications.[4] Unfortunately, compared to the electrocatalysis, low efficiency of multielectron transfer and sluggish kinetics of hydrogenation competitive steps have resulted in the rare generation of C2 intermediates to form C−C coupling product C_2H_4 in photocatalytic CO_2 reduction system.[5]

Recent studies have unveiled that Fe-based catalysts are more selective toward olefins in CO_2 conversion under high temperature and harsh pressure.[6] It is greatly desirable to engineering Fe-based catalysts with promotional C2 activity during photoreduction of CO_2 under mild conditions from a sustainability perspective. With decades of development, many strategies have been explored for synthesis and modification of catalysts, including facet controlling, interface designing, and atom doping.[7] Among them, inducing nonmetallic atom, especially heteroatom N and S, which was accompanied by defective and electronic structure recombination of catalysts, has verified vital influence on the coordination structure in MOF materials, thus changing catalytic performance to certain extent.[8] The low formation energy, abundant defects of uncoordinated atom can be a special benefit in transferring electrons to improve the charge carrier concentration.[9] Moreover, N-doped materials have been found to be promising catalysts for reduction CO_2 to multi-carbon products recently, which can act as basic sites in capture of CO_2 molecules to optimize the efficiency of charge separation to promote the dimerization of intermediates.[10] Nevertheless, on one hand, most of the previously reported synthetic approaches for N,S codoped materials are still faced with uneven distribution, noxious precursors, complicated process, and other unavoidable disadvantages.[11] On the other hand, the diverse and complex structures of N,S codoped catalysts, such as concentration, distribution, and types of introduced N,S

precursors often have disparate impact on catalytic activity, even the counter-productive.[12] Thus, to accelerate the migration of the photoelectrons and formation of the C−C coupling intermediate under mild condition, rationally design of N,S heteroatom codoped Fe-based catalysts, which include coordinated and uncoordinated sites, is crucial yet remains a challenge for practical photoreduction CO_2 to C2 products.

Herein, N,S-codoped Fe-MOF MIL-88B with a well-defined bipyramidal hexagonal prism shape was designed via a facile and simple pathway (Scheme 1). In such a strategy, 1,2-benzisothiazolin-3-one (BIT) and acetic acid were regarded as a dopant of N,S elements and a remover of original linkers, respectively. Meanwhile, the amount of BIT can regulate the generation of structure defects. Both XPS and XAS data indicate the N was introduced into MIL-88B to formulate the Fe−N sites successfully. In the modulated structures, a combination of new Fe−N active sites and more befitting defects from uncoordinated S elevates the migration and separation of the photogenerated carriers, which would lead to a high electron density at Fe catalytic sites. In turn, it helps to promote the occurrence of the multielectron reduction of CO_2. By using the N,S-codoped MIL-88B catalyst, C−C coupling product C_2H_4 was obtained with high generation rate of 17.7 μmol/g·h in the photoreduction CO_2 reaction under simulated visible light irradiation. *In situ* FT-IR spectra imply that the structure of MIL-88B with codoping suited N,S atoms is beneficial to produce the pivotal C−C coupling intermediate CH-CHOH*, which greatly improves the reduction of CO_2 to C_2H_4 in the photocatalytic process.

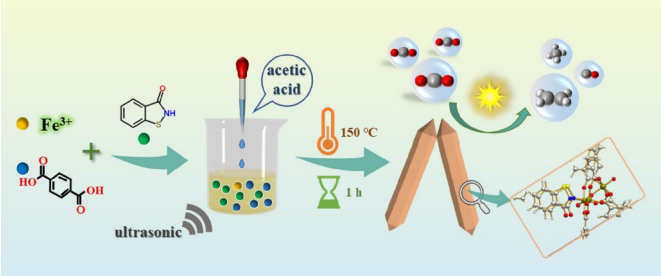

Scheme 1. Schematic illustration showing the synthetic process of N,S-codoped MIL-88B catalysts.

Results and Discussion

A series of N,S-codoped MIL-88B were obtained by introducing different amount of 1,2-benzisothiazolin-3-one (BIT) into the reaction solution via one-pot synthesis, which displayed yellowish-brown color (Figure S1). Furthermore, the ultrasonic strategy at room temperature is conducive to the metal ions and the ligands evenly distributed in the solution. In this process, BIT can not only give an extra N,S source, but also make the morphology of N,S-codoped MIL-88B unchanged. The above prepared samples with four kinds of BIT amounts are denoted as MIL-88B-NSX (x = 0, 30, 40, or 50, corresponding to the amount of BIT added).

The morphology and microstructure of the products were investigated and analyzed by scanning electron microscope (SEM), transmission electron microscopy (TEM), scanning TEM (STEM), and STEM energy-dispersive spectra (STEM−EDS). As shown in SEM images (Figure S2), the obtained samples after adding the modulator BIT exhibit the bipyramidal hexagonal prism morphology, which are consistent with pristine MIL-88B basically, but own much rough surface even with some slight cracks. The sizes of N,S-codoped MIL-88B products are all approximately 0.5 ~ 1.2 μm in width and 3 ~ 5 μm in length. The above results can be also confirmed by the TEM observation (Figure S3), and Figure 1a shows an obviously pyramid structure of MIL-88B-NS40 sample. More intuitively, the STEM and STEM−EDS elemental mapping images (Figure 1b) of MIL-88B-NS40 demonstrate that Fe (blue), N (violet), and S (yellow) elements are homogeneously distributed throughout the sample, which can provide an effective support to the successful synthesis of N and S codoped materials. These catalysts own regular morphology and large size are helpful to improve the recyclability and reusability in catalytic process.[10b] Furthermore, the acetic acid could be as the important modulator on the control of morphology for the BIT doped MIL-88B materials (Figure S4).

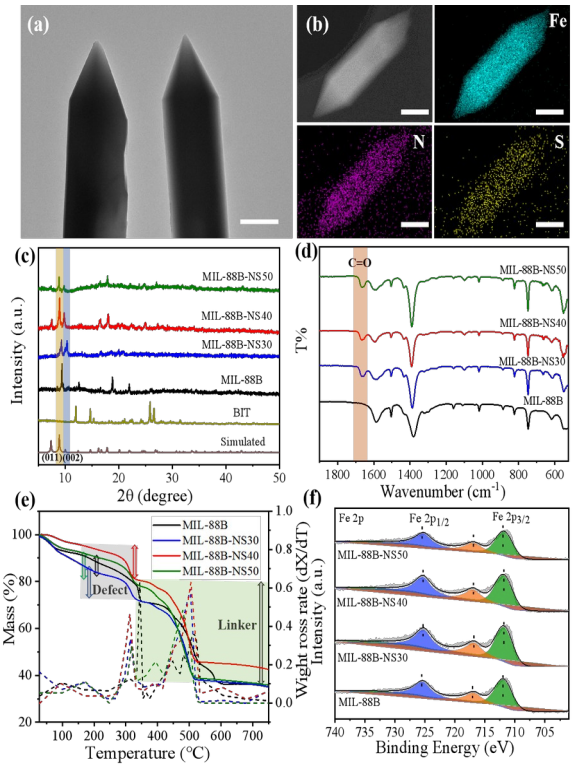

Figure 1. Morphology and structural characterization of MIL-88B-NS40 sample: (a) TEM and (b) STEM and corresponding STEM-EDX mapping images, (scale bar: 500 nm). (c) PXRD patterns, (d) FT-IR spectra, (e) TG and DTG curves (fixed color arrows in the shaded section of the upper left corner correspond to the relevant samples, respectively), and (f) High-resolution Fe 2p XPS spectra of varied catalysts.

The crystalline phases and surface functional groups of the as-prepared materials were also explored. Figure 1c shows the powder X-ray diffraction (PXRD) patterns of simulated MIL-88B and N,S-codoped MIL-88B powder. The characteristic diffraction peaks of the samples were displayed in Table S1. However, the relative intensity of diffraction peaks at 8.9° and 10.0° of N,S-codoped MIL-88B are changed, which are corresponding to (011) and (002) crystal plane, respectively, suggesting that the doping of N,S might change the exposed surface of the N,S-codoped MIL-88B.[13] Compared with the original MIL-88B, Fourier transform infrared (FT-IR) spectra show a new peak (1650 ~ 1700 cm^{-1}) in the codoped MOF materials, attributing to carbonyl group (C=O) from BIT (Figure 1d).[14] Thermogravimetric analysis (TGA) is used to measure defects for MOF materials as one of the common test method.[15] The TG and correlative derivative thermogravimetry (DTG) curves of the four samples were presented three main weight-loss steps (Figure 1e). The weight losses over the entire temperature analysis range can be assigned to the following proceeding: firstly, the weight loss of solvent molecules occurs over the temperature < 150 ºC; secondly, weight loss of corresponding ligands over the temperature range from 150 to 330 ºC; thirdly, the peaks among 330 and 500 ºC can be appointed to the completely pyrolysis of the framework. In general, the second step can be attributed to the defects degree.[16] Obviously, N,S-codoped products all own the larger magnitude of weight loss than pristine MIL-88B. More specifically, as shown in DTG curves from 150 to 330 ºC, the highest weight loss sample corresponds to MIL-88-NS40, indicating that the linker content in the structures decreases and maximum defects exist.[17] Additionally, the pore size distribution of these samples displays the typical mesoporous structures, and it is reasonable to expect the large diameters after codoping heteroatom, which can further confirm the existence of defects (Figure S5).[18]

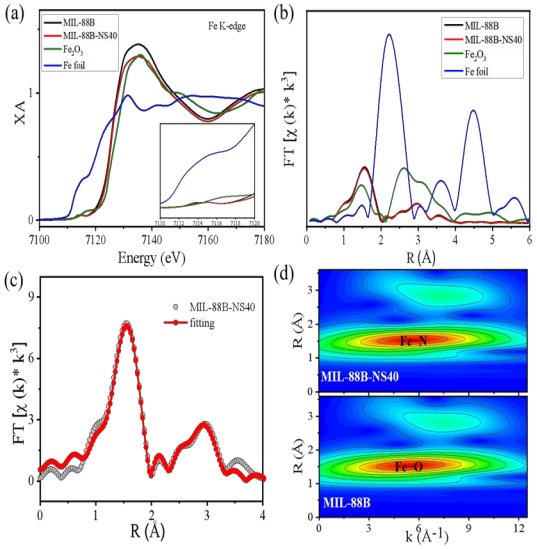

Figure 2. (a) Fe K-edge XANES and (b) FT-EXAFS spectra of MIL-88B and MIL-88B-NS40. Inset in (a) illustrates the first derivative of the XANES edge. (c) Fe K-edge EXAFS spectrum fitting of MIL-88B-NS40. (d) EXAFS WT plots of Fe in MIL-88B-NS40 and MIL-88B.

X-ray photoelectron spectroscopy (XPS) analysis was utilized to characterize the surface chemical composition and the chemical state of the catalysts. The XPS survey data of all N,S-codoped MIL-88B materials confirm the presence of N, S, O, C, and Fe elements (Figure S6 and Table S2). Compared to the MIL-88B, it can be concluded that peaks for Fe $2p_{3/2}$ and $2p_{1/2}$ in the N,S-codoped samples show different degree of negative shift from the high-resolution XPS spectra of Fe 2p (Figure 1f). Clearly, the peaks of MIL-88B-NS40 with the maximum shift reveal that the electron density around Fe site is enhanced the most, which can be attributed to its more intimate contact between the N element and Fe.[19] Likewise, this phenomenon can also be observed from the high-resolution O 1s spectra of the samples (Figure S7). Two new fitted peaks appeared in the C 1s high-resolution spectra of N,S-codoped materials compared with that of MIL-88B. For example, the four major peaks of MIL-88B-NS40 can be assigned to C=O (288.6 eV), C–N (285.7 eV, new), C=C (284.8 eV), and C–S bonds (284.3 eV, new peak) (Figure S8), demonstrating that N and S heteroatoms have been successfully incorporated into the frameworks. This consequence was highly consistent with the STEM−EDS elemental analysis results and also supported by the high-resolution N 1s and S 2p XPS spectra (Figures S9 and S10). More importantly, the new type peak of Fe–N can be observed in the high-resolution N 1s XPS spectrum for N,S-codoped MIL-88B, revealing that Fe is linked with N. Thus Fe–N coordinated sites have configured successfully after adding BIT. From the above XPS analysis, the incorporation of N,S has changed the structure of the MOF and formed the compact relationship of two components. Meanwhile, MIL-88B-NS40 may exhibits better performance because of the increased electron cloud density around Fe.[20]

In addition to the bulk structure, the local geometry around Fe center was examined by X-ray absorption spectroscopy (XAS). Figure 2a shows the X-ray absorption near-edge structure (XANES) spectra of MIL-88B and MIL-88B-NS40 at Fe K edge. The main feature observed around 7121 eV is assigned to the 1s→4p transition. Similar to the reference sample Fe_2O_3, both MIL-88B and MIL-88B-NS40 exhibit a weak pre-edge feature at 7108 eV corresponding to the quadrupole allowed 1s→3d transition, suggesting the distorted octahedral geometry of the Fe center. As shown in the first derivative spectra (Figure 2a inset), the edges of MIL-88B and MIL-88B-NS40 samples both shift slightly to lower energy compared to that of Fe_2O_3, implying that the Fe center in MOFs is dominated by +3 oxidation state but more reduced than Fe_2O_3.

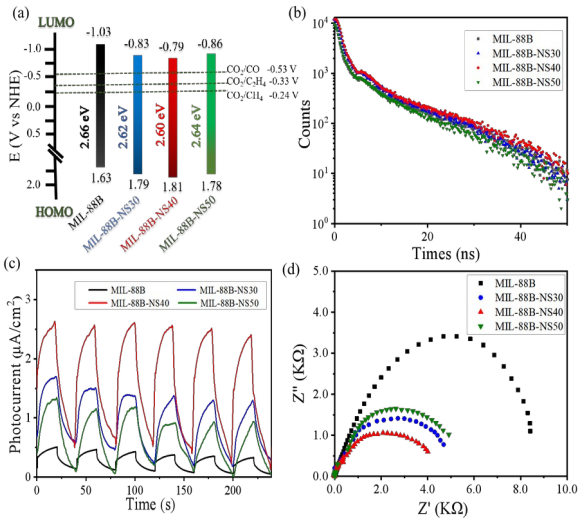

Figure 3. Comparison of (a) HOMO−LUMO gap, (b) time-resolved fluorescence decay, (c) transient photocurrent response, and (d) EIS Nyquist plots for varied catalysts.

To gain further insight into the coordination environment, extended X-ray absorption fine structure (EXAFS) spectra were quantitatively analyzed using the FeFF model. Figure 2b shows the EXAFS spectra of MIL-88B and MIL-88B-NS40 in R space. Compared to MIL-88B, the peak intensity of Fe first shell (Fe–O, Fe–N) in the spectrum of MIL-88B-NS40 is slightly reduced, which can be attributed to either decrease of the coordination number or increase disorder around Fe center.[21] It is unlikely that the coordination number of Fe center changes, which is cross verified by the XANES spectra and best fitting results. Thus the decreased peak intensity of first shell can be attributed to the increased electron density disorder due to the presence of N doping, consistent with the XPS results. Considering these analysis, structural models of MIL-88B-NS40, including coordinated Fe–N and uncoordinated S, have been constructed

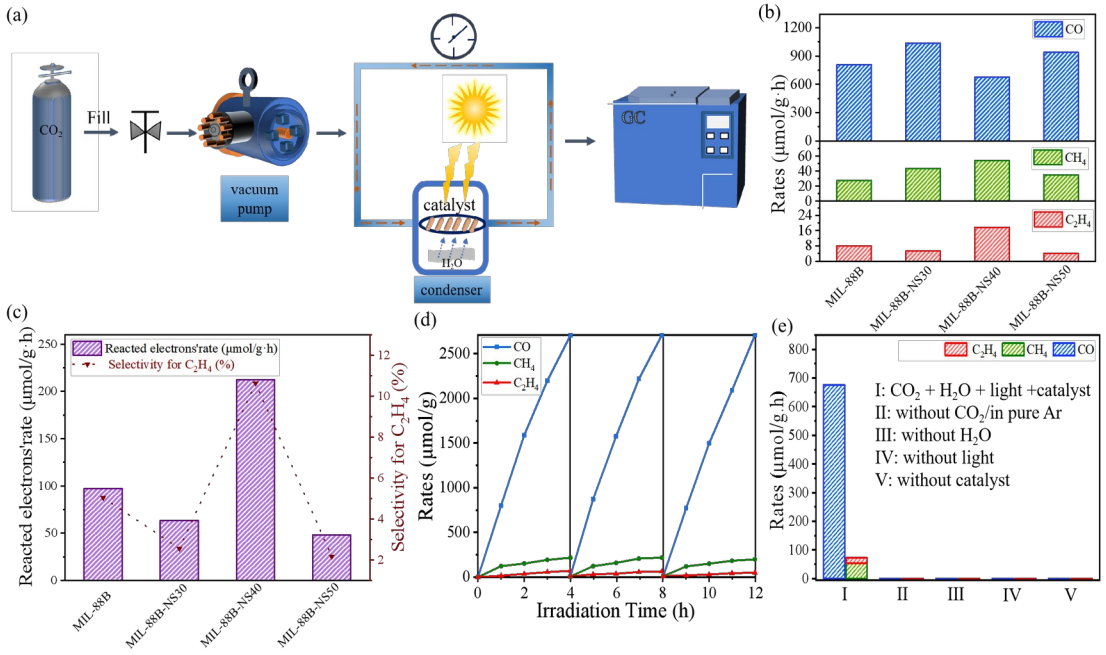

Figure 4. (a) Illustration for the photocatalytic CO_2 reduction process of N,S-codoped MIL-88B catalysts. (b) Product formation rates and (c) electron utilization selectivity of C_2H_4 for varied catalysts in the photocatalytic CO_2 reduction reaction, electron utilization selectivity of C_2H_4 (%) = (12 × v(C_2H_4)) / (2 × v(CO) + 8 × v(CH_4) + 12 × v(C_2H_4)) × 100 %. (d) Cycling measurements of sample MIL-88B-NS40. (e) Control experiments in several conditions for MIL-88B-NS40.

by simulation (Figure S11), which was also supported by the mass spectrometry (Figure S12). The best fitting of MIL-88B and MIL-88B-NS40 in R space and K space are shown in Figure S13, and Figures 2c and S14, respectively. The details of EXAFS fitting results with fitting parameters are listed in Table S3. From the best fitting, the Fe–O distance for both samples are similar (2.05 Å and 2.00 Å for MIL-88B, 2.04 Å and 1.98 Å for MIL-88B-NS40), the Fe–N distance for MIL-88B-NS40 is determined to be 1.97 Å with relatively large Debye–Waller factor, consistent with the assignment of the increased disorder. To obtain more information about the radial distance and better discriminate backscattering atoms accurately, EXAFS wavelet transform (WT) analysis was conducted. The WT analysis of MIL-88B-NS40 and MIL-88B presents the intensity maximums at around 5.4 $Å^{-1}$ and 5.3 $Å^{-1}$, which is assignable to the Fe−N and Fe−O,[22] confirming once again the grating of N on Fe nodes in MIL-88B-NS40 (Figure 2d). Thus, the XAS results strongly support the formation of Fe−N coordinated sites and the increase of electron density disorder around Fe in the structure of MIL-88B-NS40, which will play important role in the catalytic process.

In order to evaluate the feasibility of photocatalytic ability, a series of photo- and electrochemical

measurements for these catalysts were carried out. Ultraviolet-visible diffuse reflectance spectroscopy (UV-DRS) confirmed that all samples have broad absorption covering the region from ultraviolet to visible spectrum (Figure S15). Mott–Schottky (MS) measurements were further performed to determine the lowest unoccupied molecular orbital (LUMO) of the original and N,S-codoped MIL-88B materials (Figure S16). As shown in Figure S17, the highest occupied molecular orbital (HOMO)-LUMO gap edges of all synthesized samples based on the Tauc plots are corresponding to the n-type semiconductors.[23] Given the more negative the LUMO energy levels than the redox potential of CO_2 to CO [-0.53 V *vs.* normalized hydrogen electrode (NHE)], CH_4 (-0.24 V *vs.* NHE) as well as to C_2H_4 (-0.33 V *vs.* NHE),[6a] intimating that all the MIL-88B materials have capability for CO_2 photoreduction (Figure 3a). Meanwhile, the catalyst MIL-88B-NS40 with a lower HOMO–LUMO gap (2.60 eV) is more sensitive to visible light because it may requires low energy to excite photogenerated carriers.[24]

To unravel the photogenerated charge separation and transfer abilities, the corresponding characterizations were conducted. As illustrated in Figure 3b, time-resolved photofluorescence decay spectra reveal that MIL-88B-NS40 has the longest average lifetime of photogenerated charge carriers among these samples. Meanwhile, the fitted decay traces and the correlated parameters are listed in Figure S18. Therefore, the remarkable prolonged average lifetime means MIL-88B-NS40 has low recombination process, which is due to the migration of the photoelectrons more efficiently through Fe–N sites. Moreover, photocurrent response test is implemented to evaluate the separation efficiency of photoexcited charge carriers under visible light illumination. As shown in Figure 3c, MIL-88B-NS40 catalyst performs high transient photocurrent response capability compared to other samples. It is evident from the electrochemical impedance spectroscopy (EIS) that the smallest resistance for MIL-88B-NS40 demonstrates the fastest interface charge transfer rate in the Nyquist plots (Figure 3d). The above results collectively prove that Fe–N sites and more defects can be in favor of the electron storage to promote the charge separation of MIL-88B, indicating that MIL-88B-NS40 may possess the conspicuous photocatalytic activity.

Based on the above-mentioned analysis, we proceed to explore the catalytic performance of as-synthesized catalysts for CO_2 photoreduction, and the photocatalytic reaction was carried under visible light irradiation in a gas-solid reaction

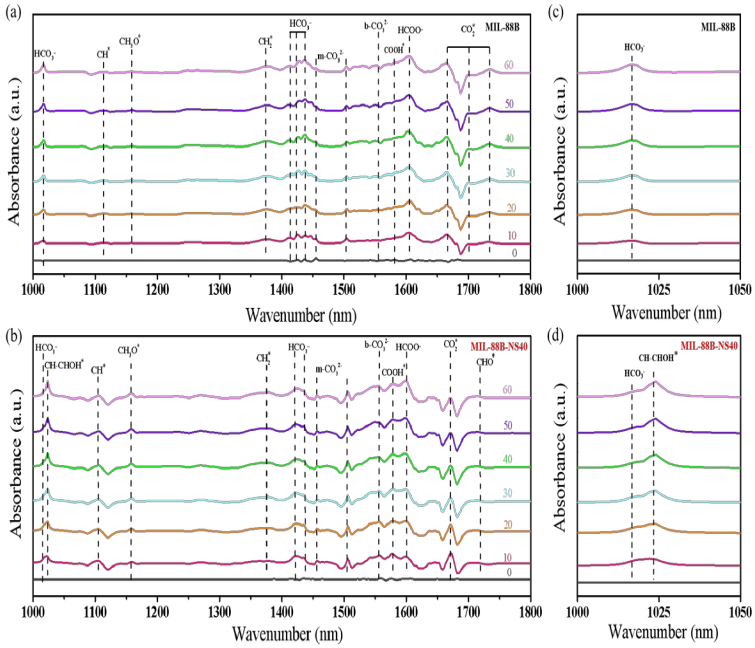

Figure 5. *In situ* FT-IR spectra of CO_2 reduction under simulated light from 0 to 60 min for (a) MIL-88B and (b) MIL-88B-NS40. Amplification of the selected wavenumber for (c) MIL-88B and (d) MIL-88B-NS40.

system (Figures 4a and S19). The catalytic results of pristine bipyramidal hexagonal prism and varied N,S codoped MIL-88B catalysts were displayed in Figure 4b and Table S4, and the liquid products are inexistence under observation (Figure S20). Notably, the yields of products for CO_2 reduction are closely related to the

amount of N,S incorporated. The samples MIL-88B-NS30 and MIL-88B-NS50 exhibit appreciably increased rates of CO and CH_4 production compared with MIL-88B, indicating smaller quantity of defects in the structures of MIL-88B are beneficial to enhance the C1 products. Intriguingly, except C1 products of CO and CH_4 reduced from CO_2 by the catalyst MIL-88B-NS40, high rate of C2 hydrocarbon product C_2H_4 (17.7 μmol/g·h) was also detected, which was rarely been achieved in reported photocatalytic reaction systems (Table S5). The high evolution yields of C_2H_4 and CH_4 are almost doubled of MIL-88B, but opposite trend as that of CO, demonstrating MIL-88B-NS40 is more favorable to the generation of multielectron-reduced hydrocarbons of CH_4 and C_2H_4. The electron selectivity of hydrocarbon productions can achieve 32.3%, with around 10.6% C2 production (Figure 4c). Thus, we suggest that C–C coupling takes place more efficiently on the MIL-88B-NS40 catalyst, due to its suited Fe–N active sites and more defects from uncoordinated S in the structure.

Moreover, the CO_2 temperature-programmed desorption (TPD) measurement is a convincing technique to explore the strength of basic sites on the surface of the materials, evaluating the interaction force between CO_2 molecules and the catalysts.[25] Both MIL-88B and MIL-88B-NS40 show a strong desorption peak in the CO_2-TPD profile, while the desorption temperature of MIL-88B-NS40 (294 ºC) is higher than MIL-88B (290 ºC) (Figure S21). On account of the basic strength of the catalyst is inextricably associated with desorption temperature in the CO_2-TPD, the higher desorption temperature manifests more Lewis basic sites at the surface of MIL-88B-NS40.[26] This behavior can be a proof that the regulated combination of MIL-88B with N,S is conducive to enhancing the binding capacity toward CO_2. The electron paramagnetic resonance (EPR) spectral measurement was conducted to unveil the charge transfer behavior (Figure S22). When visible light is irradiated on the above reaction system, compared with MIL-88B, MIL-88B-NS40 exhibits enhanced EPR signal ascribed to Fe^{3+},[27] which can be well explained by the enhanced charge transfer due to the rational structural defects. The above result is in agreement with the photocatalytic experiment, in which MIL-88B-NS40 shows increased selectivity and reactivity for CO_2 reduction reaction. Furthermore, recycling experiments were used to assess the photostability of MIL-88B-NS40, as shown in Figure 4d, after three times uninterrupted cycles, MIL-88B-NS40 still maintains catalytic activity. The PXRD patterns suggest that the structure of MIL-88B-NS40 has no noticeable alteration after the photocatalytic reaction (Figure S23), and the high stability may attribute to the regular morphology and large size of the catalyst.[10b] Meanwhile, as displayed in Figure S24, the higher quantum efficiency (QE) values of C_2H_4 and CH_4 evolution for MIL-88B-NS40 under varied monochromatic light wavelength indicate that the appropriate N,S codoped structures endow the photocatalyst in favor of reducing CO_2 to multielectron hydrocarbons. Under the identical conditions, appearance of C_2H_4, CH_4, and CO was not detected in a series of blank experiments without light, catalyst, or H_2O, and so on (in Figure 4e). For example, in the absence of CO_2 no products detected testify that the carbon source was entirely from the preliminary input CO_2 rather than other sources. Additionally, the same result can also be supported by the labeling $^{13}CO_2$ experiment and the signals at m/z = 30, m/z = 29 and m/z = 17 corresponding to the reaction products $^{13}C_2H_4$, ^{13}CO, and $^{13}CH_4$ were detected by gas chromatography−mass spectrometry (GC−MS) (Figure S25).

To deeply understand the reaction path and possible intermediates of CO_2 photocatalytic reduction, *in situ* FT-IR spectroscopy was used to investigate the adsorption and conversion process of CO_2 on MIL-88B and MIL-88B-NS40 (Figure S26). All FT-IR peak intensities gradually increase with extension of the time. As shown in Figures 5a and 5b, under simulated light, the peaks around 1018, 1420 and 1434 cm^{-1} of the above samples indicate that the HCO_3^- intermediate is present.[27] The characteristic peak around 1580 cm^{-1} can be ascribed to COOH*, which is the crucial intermediate for reducing CO_2 to C1 and multi-carbon products.[28] Meanwhile, the characteristic peak between about 1662 and 1702 cm^{-1} is assigned to CO_2*.[29] The relative stronger peak intensities for MIL-88B-NS40 compared with MIL-88B, including CH* (1108 cm^{-1}), CH_3O* (1159 cm^{-1}), and CH_2* (1375 cm^{-1}), reflect that the incorporated N,S in structure of MIL-88B-NS40 is conducive to the product of C_2H_4 and CH_4.[30] Furthermore, the peaks at ~1557 cm^{-1} and 1600 cm^{-1} are assigned to the $HCOOH^-$ and bidentate carbonates (b-CO_3^{2-}),[31] respectively, and those at about 1456 and 1504 cm^{-1} correspond to monodentate carbonate (m-CO_3^{2-}).[32] Several new intermediate groups CHO* (1714 cm^{-1}), and in particular, C–C coupling CH-CHOH* (1024 cm^{-1}) for MIL-88B-NS40 (Figures 5c and 5d), demonstrate more probability of producing multi-carbon product for MIL-88B-NS40 than MIL-88B.[30],[33] Therefore, coordinated Fe–N active sites and befitting defects from uncoordinated S in MIL-88B-NS40 catalyst synergistically promote the reduction of CO_2 molecules to generate the CH-CHOH* dimerization for C–C coupling products. Based on the *in situ* FT-IR spectra analysis, the most possible reaction path of reduction CO_2 to CO, CH_4, and C_2H_4 for MIL-88B-NS40 in the catalytic system is described in Figure S27.

Conclusion

In this work, a design strategy for codoping N,S into MIL-88B was developed via one-pot method conveniently. A series of control tests indicate that the MIL-88B-NS40 catalyst has promotional catalytic property for reducing CO_2 to C2 product C_2H_4 (17.7 μmol/g·h) under simulated sunlight, which can be comparable with most reported photocatalysts own high activity. Synergistically deigning of established Fe−N sites and proper defects from uncoordinated S play critical role in the electron delivery more efficiently, further boost the possibility of the multielectron reduction process. On the basis of *in situ* FT-IR characterization, the structure in MIL-88B-NS40

facilitates the generation of C−C coupling dimerization, thus greatly enhancing the photoreduction of CO_2 to C_2H_4. Our study provides a promising approach to achieve the generation of C2 hydrocarbon product from CO_2 reduction in a photocatalytic system.

Acknowledgements

We gratefully acknowledge the National Natural Science Foundation of China (grant nos. 22101246, 22231006 and 22171131) for financial support of this work. This work was also supported by a Project Funded by the Priority Academic Program Development of Jiangsu Higher Education Institutions. F. Guo acknowledges the Double Innovation Doctor Program of Jiangsu Province (No. JSSCBS20211022) and the Green Yang Jinfeng Talent Project of Yangzhou (No. YZLYJF2020PHD057).

Keywords: codope • defect • metal–organic frameworks • photocatatic CO_2 • C_2H_4

[1] a) B. Obama, *Science* **2017**, *355*, 126-129; b) J.-W. Yoon, J.-H. Kim, C. Kim, H. W. Jang, J.-H. Lee, *Adv. Energy Mater.* **2021**, *11*, 2003052.

[2] a) Y.-C. Hao, L.-W. Chen, J. Li, Y. Guo, X. Su, M. Shu, Q. Zhang, W.-Y. Gao, S. Li, Z.-L. Yu, L. Gu, X. Feng, A.-X. Yin, R. Si, Y.-W. Zhang, B. Wang, C.-H. Yan, *Nat. Comm.* **2021**, *12*, 2682; b) L.-Y. Wu, Y.-F. Mu, X.-X. Guo, W. Zhang, Z.-M. Zhang, M. Zhang, T.-B. Lu, *Angew. Chem. Int. Ed.* **2019**, *58*, 9491-9495; *Angew. Chem.* **2019**, *131*, 9591-9595; c) F. Guo, M. Yang, R.-X. Li, Z.-Z. He, Y. Wang, W.-Y. Sun, *ACS Catal.* **2022**, *12*, 9486-9493; d) H. Rao, L. C. Schmidt, J. Bonin, M. Robert, *Nature* **2017**, *548*, 74-77.

[3] a) W. Jiang, J. Low, K. Mao, D. Duan, S. Chen, W. Liu, C.-W. Pao, J. Ma, S. Sang, Chang Shu, X. Zhan, Z. Qi, H. Zhang, Z. Liu, X. Wu, R. Long, L. Song, Y. Xiong, *J. Am. Chem. Soc.* **2021**, *143*, 269-278; b) C. Choi, S. Kwon, T. Cheng, M. Xu, P. Tieu, C. Lee, J. Cai, H. M. Lee, X. Pan, X. Duan, W. A. Goddard, Y. Huang, *Nat. Catal.* **2020**, *3*, 804-812.

[4] a) Y. Jiang, D. Zhong, L. Wang, J, Li, G, Hao, J, Li, Q, Zhao, *Chem. Eur. J.* **2022**, *17*, e202200380; b) D.-H. Nam, O. S. Bushuyev, J. Li, P. D. Luna, A. Seifitokaldani, C.-T. Dinh, F. P. G. d. Arquer, Y. Wang, Z. Liang, A. H. Proppe, C. S. Tan, P. Todorović, O. Shekhah, C. M. Gabardo, J. W. Jo, J. Choi, M.-J. Choi, S.-W. Baek, J. Kim, D. Sinton, S. O. Kelley, M. Eddaoudi, E. H. Sargent, *J. Am. Chem. Soc.* **2018**, *140*, 11378-11386: c) 11.Y. Zhang, Q. Zhou, Z.-F. Qiu, X.-Y. Zhang, J.-Q. Chen, Y. Zhao, F. Gong, W.-Y. Sun, *Adv. Funct. Mater.* **2022**, 2203677.

[5] a) L. Yuan, M.-Y. Qi, Z.-R. Tang, Y.-J. Xu, *Angew. Chem. Int. Ed.* **2021**, *60*, 2-25; *Angew. Chem.* **2021**, *133*, 21320-21342; b) W. Wang, C. Deng, S. Xie, Y. Li, W. Zhang, H. Sheng, C. Chen, J. Zhao, *J. Am. Chem. Soc.* **2021**, *143*, 2984-2993.

[6] a) J. Albero, Y. Peng, H. García, *ACS Catal.* **2020**, *10*, 5734-5749; b) Z. Li, J. Liu, R. Shi, G. I. N. Waterhouse, X.-D. Wen, T. Zhang, *Adv. Energy Mater.* **2021**, *11*, 2002783.

[7] a) Y. Wang, Z. Wang, C.-T. Dinh, J. Li, A. Ozden, M. G. Kibria, A. Seifitokaldani, C.-S. Tan, C. M. Gabardo, M. Luo, H. Zhou, F. Li, Y. Lum, C. McCallum, Y. Xu, M. Liu, A. Proppe, A. Johnston, P. Todorovic, T.-T. Zhuang, D. Sinton, S. O. Kelley, E. H. Sargent, *Nat. Catal.* **2020**, *3*, 98-106; b) Z.-Z. Wu, X.-L. Zhang, Z.-Z. Niu, F.-Y. Gao, P.-P. Yang, L.-P. Chi, L. Shi, W.-S. Wei, R. Liu, Z. Chen, S. Hu, X. Zheng, M.-R. Gao, *J. Am. Chem. Soc.* **2022**, *144*, 259-269; c) C. Xie, D. Yan, H. Li, S. Du, W. Chen, Y. Wang, Y. Zou, R. Chen, S. Wang, *ACS Catal.* **2020**, *10*, 11082-11098.

[8] a) J. Jin, P. Li, D. H. Chun, B. Jin, K. Zhang, J. H. Park, *Adv. Funct. Mater.* **2021**, *31*, 2102511; b) E. Pastor, M. Sachs, S. Selim, J. R. Durrant, A. A. Bakulin, A. Walsh, *Nat. Revie. Mater.* **2022**, *7*, 503-521.

[9] C. Chen, X. Wang, Z. Li, X. Du, Z. Shao, X. Sun, D. Liu, C. Gao, L. Hao, Q. Zhao, B. Zhang, G. Cui, S. Pang, *Angew. Chem. Int. Ed.* **2022**, *61*, e202113932; *Angew. Chem.* **2022**, *134*, e202113932.

[10] a) J. Wu, S. Ma, J. Sun, J. I. Gold, C. Tiwary, B. Kim, L. Zhu, N. Chopra, I. N. Odeh, R. Vajtai, A. Z. Yu, R. Luo, J. Lou, G. Ding, P. J. Kenis, P. M. Ajayan, *Nat. Commun.* **2016**, *7*, 13869; b) L. Sun, R. Li, W. Zhan, Y. Yuan, X. Wang, X. Han, Y. Zhao, *Nat. Commu.* **2019**, *10*, 2270.

[11] a) Y. Xue, B. Wu, L. Jiang, Y. Guo, L. Huang, J. Chen, J. Tan, D. Geng, B. Luo, W. Hu, G. Yu, Y. Liu, *J. Am. Chem. Soc.* **2012**, *134*, 11060-11063; b) X. Cui, S. Yang, X. Yan, J. Leng, S. Shuang, P. M. Ajayan, Z. Zhang, *Adv. Funct. Mater.* **2016**, *26*, 5708-5717.

[12] Yan, D.; Li, H.; Chen, C.; Zou, Y.; Wang, S. *Small Methods* **2019**, *3*, 1800331.

[13] Z. Qu, Y. Muhammad, W. T. He, J. L. Li, Z. Gao, J. H. Fu, S. J. Shah, H. J. Sun, J. X. Wang, Z. Q. Huang, Z. X. Zhao, *Chem. Eng. J.* **2021**, *404*, 126570.

[14] L. Pukdeejorhor, K. Adpakpang, P. Ponchai, S. Wannapaiboon, S. Ittisanronnachai, M. Ogawa, S. Horike, S. Bureekaew, *Cryst. Growth Des.* **2019**, *19*, 5581-5591.

[15] G. C. Shearer, S. Chavan, S. Bordiga, S. Svelle, U. Olsbye, K. P. Lillerud, *Chem. Mater.* **2016**, *28*, 3749-3761.

[16] S. Dissegna, K. Epp, W. R. Heinz, G. Kieslich, R. A. Fischer, *Adv. Mater.* **2018**, *30*, 1704501.

[17] X. Feng, H. S. Jena, C. Krishnaraj, D. Arenas-Esteban, K. Leus, G. Wang, J. Sun, M. Rüscher, J. Timoshenko, B. R. Cuenya, S. Bals, P. V. D. Voort, *J. Am. Chem. Soc.* **2021**, *143*, 21511-21518.

[18] X. Ma, L. Wang, Q. Zhang, H.-L. Jiang, *Angew. Chem. Int. Ed.* **2019**, *58*, 12175-12179; *Angew. Chem.* **2019**, *131*, 12303-12307.

[19] a) X. Li, X. Yang, L. Liu, H. Zhao, Y. Li, H. Zhu, Y. Chen, S. Guo, Y. Liu, Q. Tan, G. Wu, *ACS Catal.* **2021**, *11*, 7450-7459; b) Tan, A. D.; Wan, K.; Wang, Y. F.; Fu, Z. Y.; Liang, Z. X. N, *Catal. Sci. Technol.* **2018**, *8*, 335-343.

[20] a) L. Li, J.-D. Yi, Z.-B. Fang, X.-S. Wang, N. Liu, Y.-N. Chen, T-F Liu, R. Cao. *Chem. Mater.* **2019**, *31*, 7584-7589; b) Y. Jiang, Y.-P. Deng, R. Liang, N. Chen, G. King, A. Yu, Z. Chen, *J. Am. Chem. Soc.* **2022**, *144*, 4783-4791.

[21] Y. Wang, J. Wang, D. Wei, M. Li, *ACS Appl. Mater. Interfaces* **2019**, *11*, 35755-35763.

[22] a) L. Jiao, J. Zhu, Y. Zhang, W. Yang, S. Zhou, A. Li, C. Xie, X. Zheng, W. Zhou, S.-H. Yu, H.-L. Jiang, *J. Am. Chem. Soc.* **2021**, *143*, 19417-19424; b) P. Sun, K. Qiao, D. Li, X. Liu, H. Liu, L. Yang, H. Xu, Z. Zhuang, Y. Yan, D. Cao, *Chem Catalysis* **2022**, *2*, 1-14.

[23] Z.-H. Yan, M.-H. Du, J. Liu, S. Jin, C. Wang, G. L. Zhuang, X.-J. Kong, L.-S. Long, L.-S. Zheng, *Nat. Commun.* **2018**, *9*, 3353.

[24] a) F. Yu, X. Jing, Y. Wang, M. Sun, C. Duan, *Angew. Chem. Int. Ed.* **2021**, *60*, 24849-24853; *Angew. Chem.* **2021**, *133*, 25053-25057: b) J. Ji, R. Li, H. Zhang, Y. Duan, Q. Liu, H. Wang, Z. Shen, *Appl. Catal. B: Environ.* **2023**, *321*, 122020.

[25] D. Wang, Z. Li. *Catal. Sci. Technol.* **2015**, *5*, 1623-1628.

[26] X. Zhao, S. Li, H. Cheng, J. Schmidt, A. Thomas, *ACS Appl. Mater. Interfaces* **2018**, *10*, 3912-3920.

[27] D. Wang, R. Huang, W. Liu, D. Sun, Z. Li, *ACS Catal.* **2014**, *4*, 4254-4260.

[28] C. Zhu, X. Wei, W. Li, Y. Pu, J. Sun, K. Tang, H. Wan, C. Ge, W. Zou, L. Dong, *ACS Sustainable Chem. Eng.* **2020**, *8*, 14397-14406.

[29] a) N. J. Firet, W. A. Smith, *ACS Catal.* **2017**, *7*, 606-612. b) Xu, J. Z. Ju, W. Zhang, Y. Pan, J. Zhu, J. Mao, X. Zheng, H. Fu, M. Yuan, H. Chen, R. Li, *Angew. Chem. Int. Ed.* **2021**, *60*, 8787-8791; *Angew. Chem.* **2021**, *133*, 8787-8791.

[30] H. Yu, J. Li, Y. Zhang, S. Yang, K. Han, F. Dong, T. Ma, H. Huang, *Angew. Chem. Int. Ed.* **2019**, *58*, 3880-3884; *Angew. Chem.* **2019**, *131*, 3920-3924.

[31] a) W. Gao, S. Li, H. He, X. Li, Z. Cheng, Y. Yang, J. Wang, Q. Shen, X. Wang, Y. Xiong, Y. Zhou, Z. Zou, *Nat. Commun.* **2021**, *12*, 4747; b) X. Li, Y. Sun, J. Xu, Y. Shao, J. Wu, X. Xu, Y. Pan, H. Ju, J. Zhu, Y Xie, *Nat. Energy* **2019**, *4*, 690-699.

[32] Y. Yu, X. Dong, P. Chen, Q. Geng, H. Wang, J. Li, Y. Zhou, F. Dong, *ACS Nano* **2021**, *15*, 14453-14464.

[33] M. Wang, M. Shen, X. Jin, J. Tian, M. Li, Y. Zhou, L. Zhang, Y. Li, J. Shi, *ACS Catal.* **2019**, *9*, 4573-4581.

[34] a) E. Pérez-Gallent, M. C. Figueiredo, F. Calle-Vallejo, M.T. M. Koper, *Angew. Chem. Int. Ed.* **2017**, *56*, 3621-3624; *Angew. Chem.* **2017**, *129*, 3675-3678; b) Y. Zhou, B. S. Yeo, *J. Mater. Chem. A* **2020**, *8*, 23162-23186.

Entry for the Table of Contents

Designing Heteroatom-Codoped Iron Metal–Organic Framework for Promotional Photoreduction of Carbon Dioxide to Ethylene

Fan Guo, Rui-Xia Li, Sizhuo Yang, Xiao-Yu Zhang, Hongjian Yu, Jeffrey J. Urban, and Wei-Yin Sun**

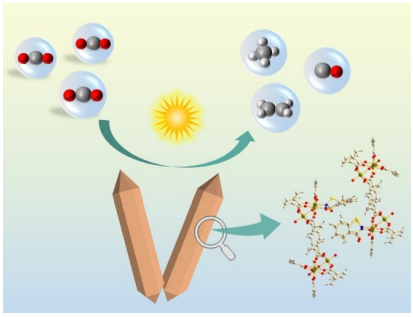

This work demonstrates the integration of new active sites with more befitting defects in Fe-MOF MIL-88 catalysts for enhanced photoreduction of CO_2 to C_2H_4 under visible light, and the modified structure elevates the migration and separation of the photoelectrons to produce the pivotal C−C coupling intermediate for the generation of C_2H_4 supported by *In situ* FT-IR analysis.